The dust environment of comet 67P/Churyumov–Gerasimenko: results from Monte Carlo dust tail modelling applied to a large ground-based observation data set

Journal Item

Monthly Notices of the ROYAL ASTRONOMICAL SOCIETY

MNRAS **469,** S186–S194 (2017) doi:10.1093/mnras/stx1424
Advance Access publication 2017 June 12

The dust environment of comet 67P/Churyumov–Gerasimenko: results from Monte Carlo dust tail modelling applied to a large ground-based observation data set

Fernando Moreno,[1]★ Olga Muñoz,[1] Pedro J. Gutiérrez,[1] Luisa M. Lara,[1] Colin Snodgrass,[2] Zhong Y. Lin,[3] Vincenzo Della Corte,[4,5] Alessandra Rotundi[4,5] and Masafumi Yagi[6]

[1]*Instituto de Astrofísica de Andalucía, CSIC, Glorieta de la Astronomía s/n, E-18008 Granada, Spain*
[2]*School of Physical Sciences, The Open University, Walton Hall, Milton Keynes, MK7 6AA, UK*
[3]*National Central University, No.300 Jhongda Rd., Jhongli City, Taoyuan County 320, Taiwan*
[4]*INAF - Istituto di Astrofisica e Planetologia Spaziali, via del Fosso del Cavaliere, 100, Roma I-00133, Italy*
[5]*Dipartimento di Scienze e Tecnologie, Università degli Studi di Napoli 'Parthenope', Centro Direzionale di Napoli isola C4, Napoli I-80143, Italy*
[6]*Optical and Infrared Astronomy Division, National Astronomical Observatory of Japan, 2-21-1, Osawa, Mitaka, Tokyo 181-8588, Japan*

Accepted 2017 June 6. Received 2017 June 5; in original form 2017 March 30

ABSTRACT

We present an extensive data set of ground-based observations and models of the dust environment of comet 67P/Churyumov–Gerasimenko covering a large portion of the orbital arc from about 4.5 au pre-perihelion through 3.0 au post-perihelion, acquired during the current orbit. In addition, we have also applied the model to a dust trail image acquired during this orbit, as well as to dust trail observations obtained during previous orbits, in both the visible and the infrared. The results of the Monte Carlo modelling of the dust tail and trail data are generally consistent with the *in situ* results reported so far by the *Rosetta* instruments Optical, Spectroscopic, and Infrared Remote Imaging System (OSIRIS) and Grain Impact Analyser and Dust Accumulator (GIADA). We found the comet nucleus already active at 4.5 au pre-perihelion, with a dust production rate increasing up to $\sim$3000 kg s^{-1} some 20 d after perihelion passage. The dust size distribution at sizes smaller than $r = 1$ mm is linked to the nucleus seasons, being described by a power law of index -3.0 during the comet nucleus southern hemisphere winter but becoming considerably steeper, with values between -3.6 and -4.3, during the nucleus southern hemisphere summer, which includes perihelion passage (from about 1.7 au inbound to 2.4 au outbound). This agrees with the increase of the steepness of the dust size distribution found from GIADA measurements at perihelion showing a power index of -3.7. The size distribution at sizes larger than 1 mm for the current orbit is set to a power law of index -3.6, which is near the average value of *insitu* measurements by OSIRIS on large particles. However, in order to fit the trail data acquired during past orbits previous to the 2009 perihelion passage, a steeper power-law index of -4.1 has been set at those dates, in agreement with previous trail modelling. The particle sizes are set at a minimum of $r = 10$ μm, and a maximum size, which increases with decreasing heliocentric distance, in the 1–40 cm radius domain. The particle terminal velocities are found to be consistent with the *in situ* measurements as derived from the instrument GIADA on board *Rosetta*.

Key words: Methods: numerical – Comets: general – Comets: individual: 67P.

1 INTRODUCTION

The European Space Agency's outstanding *Rosetta* mission has produced a historic legacy of data on the Jupiter Family Comet 67P/Churyumov–Gerasimenko (hereafter 67P). While *in situ* data produce invaluable information on the dust environment, large-scale observations from the ground provide complementary information, particularly on dust properties, allowing us to infer the total dust production rates and to observe the dust coma and tail at huge distances compared to *Rosetta*'s orbits. The observations described in this paper, part of an international ground-based observational

*E-mail: fernando@iaa.es

Table 1. Overview of telescopes and instrument/detectors used.

Observatory	Telescope	Detector	FoV (arcmin × arcmin)	Scale (arcsec px^{-1})
ESO	VLT (8.2-m)	FORS2	6.8×6.8	0.25
LULIN	SLT (0.4-m)	CCD	27×27	0.79
MAUNA KEA	Subaru (8.2-m)	HSC	90×90	0.169
CAHA	2.2-m	CAFOS	16× 16[1]	0.53[2]
CAHA	3.5-m	MOSCA	11×11	0.32
OSN	0.90-m	CCD	13×13	0.77
OSN	1.52-m	CCD	7.8×7.8	0.46

Notes. [1]32arcmin × 32arcmin in full frame mode.
[2]1.06arcsec px^{-1} in full frame mode.

campaign (Snodgrass et al. 2017), cover quite a large portion of the orbital arc of 67P while it was active. The comet was available for observation from the southern skies from 2014 February (at heliocentric distances of 4.5 au inbound) through 2014 November. Then, after a period of low solar elongation, the comet was observable again from 2015 April from the Northern hemisphere.

In this paper, we describe the optical images taken from the Very Large Telescope (VLT) on Cerro Paranal, Chile, the Lulin Observatory in Taiwan, the Subaru telescope in Mauna Kea, Hawaii, USA, and the Centro Astronómico Hispano-Alemán (CAHA) in Calar Alto and Sierra Nevada (OSN) observatories in Spain. In total, the comet was observed on 116 dates in the period 2014 February through 2016 June. All the data were simulated with a Monte Carlo dust tail code in order to extract the dust physical properties and their evolution with heliocentric distance, checking their compatibility with *Rosetta* results. The observation with Subaru telescope was particularly useful because it captured the dust trail. This observation was combined with older images of the trail obtained during the previous 67P orbit to constrain the size distribution of large particles ejected from the nucleus.

2 OBSERVATIONS AND DATA REDUCTION

Images of 67P dust tail have been recorded from several observatories/telescopes as follows. In all cases (except the observation with Subaru telescope, in which a Sloan *g*-band filter was employed), *R*-band filters were used in order to avoid the UV and blue portion of the comet spectrum where the most intense emission bands take place. A stack or median combined image of all the available frames was obtained for each night. Pre-perihelion images at far heliocentric distances were acquired using the Focal Reducer and low dispersion Spectrograph 2 (FORS2) on the VLT. These data were already described and analysed by Snodgrass et al. (2016) and Moreno et al. (2016a), in combination with images obtained by *Rosetta*/OSIRIS (the Optical, Spectroscopic, and Infrared Remote Imaging System camera; Keller et al. 2007) during *Rosetta*'s approach phase. Owing to the small solar elongation angles, no observations could be secured in the range of heliocentric distances between 2.5 and 1.4 au pre-perihelion. Just before perihelion, from 2015 June to August, CCD images were acquired using the Lulin Observatory 0.4-m Super-light Telescope (SLT) in Taiwan. At perihelion, and later, the 2.2- and 3.5-m telescopes at CAHA were used, as well as the 1.52- and 0.9-m telescopes at the Observatorio de Sierra Nevada. The instrumentation used at CAHA was the Calar Alto Faint Object Spectrograph (CAFOS) at the 2.2-m telescope, and the Multi Object Spectrograph for Calar Alto (MOSCA) at the 3.5-m telescope. Table 1 gives a summary of the instrumentation and detectors used.

Table 2 (available online) summarizes the log of the observations, where the observing dates are indicated along with the relevant geometric parameters. The images were conveniently calibrated using the *R*-band magnitude data shown by Snodgrass et al. (2016) (see their fig. 10) which are very reliable because measurements from several observatories are seen to converge on a well-defined curve. These magnitudes refer to a 10^4 km aperture radius centred at the predicted nucleus position. These magnitude data were converted to the corresponding Afρ values (with $\rho = 10^4$ km; A'Hearn et al. 1984), that were used as fitting parameters for the modelling of the data as will be shown later. A sample of representative images obtained at different observatories is given in Fig. 1.

3 THE MODEL

To carry out a theoretical interpretation of the dust tail images in terms of the physical parameters of the dust, we used our Monte Carlo dust tail code. This code has been thoroughly used in several applications, including comets and activated asteroids (for recent applications, see e.g. Moreno et al. 2016a,b). This model computes the dust tail brightness of a comet, or activated asteroid, by adding up the contribution to the brightness of each particle ejected from the parent nucleus. The particles, after leaving the object's surface, are ejected to space experiencing the solar gravity and radiation pressure. The nucleus gravity force is neglected, a valid approximation for small-sized objects, such as comet 67P. Then, the trajectory of the particles becomes Keplerian, having orbital elements, depending on their physical properties and their terminal velocities (e.g. Fulle 1989), i.e. the velocity reached by the particles at $\sim 20R_N$ (R_N is the nucleus radius), where the gas drag vanishes. In order to build up a usable representation of the synthetic images with the Monte Carlo procedure, we usually launch from 2×10^6 to 2×10^7 particles for each individual image. We assume that the particles are isotropically ejected from the surface of the $20R_N$ sphere. In fact, anisotropic ejection patterns, although they can be implemented in the model, are very difficult to be defined due to the highly time-dependent anisotropic outgassing patterns and transient events, as revealed by the OSIRIS images (e.g. Lara et al. 2015; Lin et al. 2015; Vincent et al. 2016).

The ratio of radiation pressure to the gravity forces exerted on each particle is given by the parameter $\beta = C_{pr}Q_{pr}/(2\rho r)$, where $C_{pr} = 1.19\times 10^{-3}$ kg m^{-2}, Q_{pr} is the radiation pressure coefficient and ρ is the particle density. Q_{pr} is taken as 1, as it converges to that value for absorbing particles of radius $r \gtrsim 1$ μm (see e.g. Moreno et al. 2012, their fig. 5).

To make the problem tractable, we have to adopt some of the model parameters as fixed quantities. In addition, the *in situ* determination of various key parameters by *Rosetta* instruments narrows the range of the input parameters. Two physical parameters concerning the intimate nature of the particles, namely the density and the geometric albedo, are held fixed to the values determined from the Grain Impact Analyser and Dust Accumulator (GIADA; Colangeli et al. 2007) and OSIRIS measurements, i.e. $\rho_d = 800$ kg m^{-3} and $p_v = 0.065$ (Fulle et al. 2016b; Fornasier et al. 2015). For the particle phase function correction, we use a linear phase coefficient of 0.03 mag deg^{-1}, which is in the range of comet dust particles in the $1 \leq \zeta \leq 30$ deg phase angle domain (Meech & Jewitt 1987). A broad size distribution is assumed, with a minimum, time-independent, particle radius set to 10 μm. This choice is motivated by the very few sub-micron and micrometer particles that have been collected by MIDAS (the Micro-Imaging Dust Analysis System on board *Rosetta*; Riedler et al. 2007), much less than

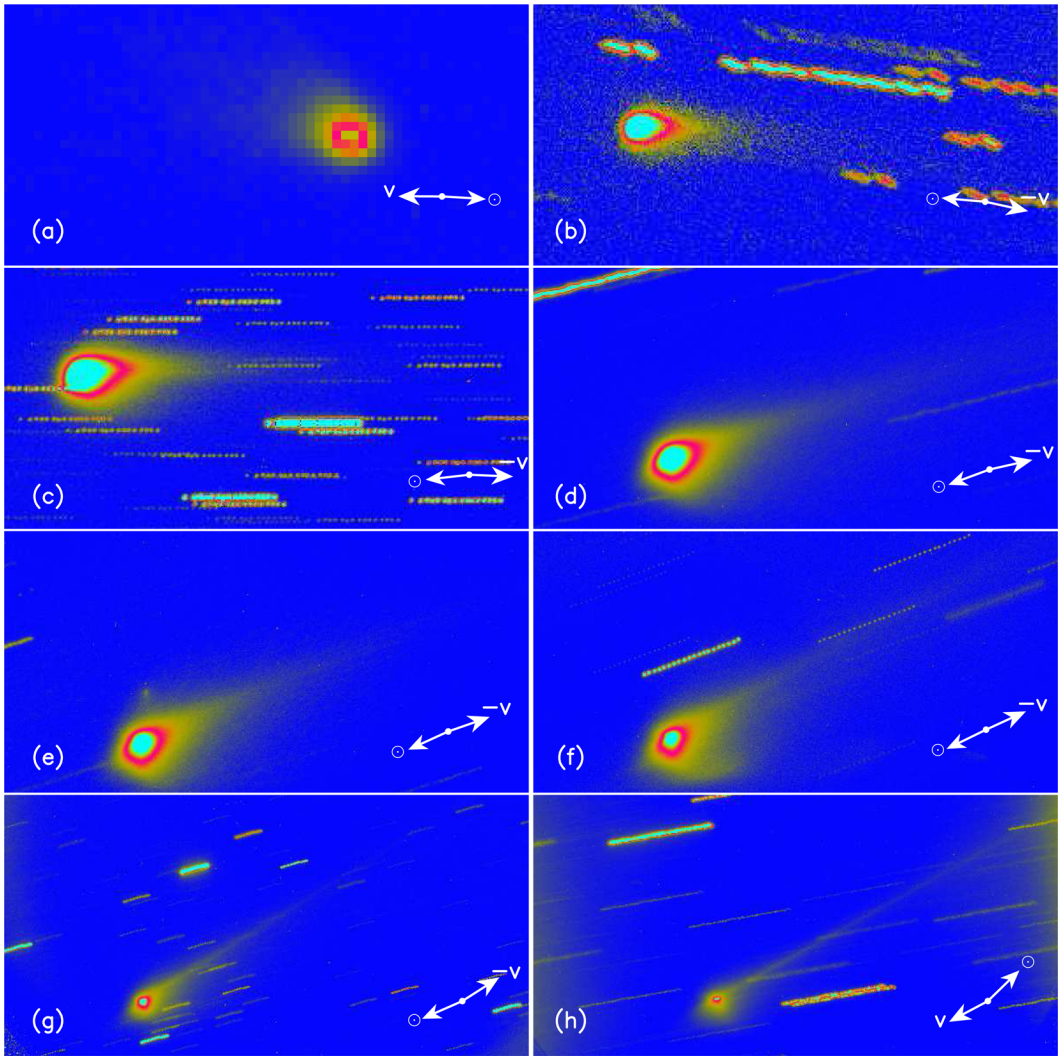

Figure 1. Set of representative images of 67P acquired at the following observatories and dates: (a) VLT, 2014-10-24, $r_h = 3.12$ au inbound; (b) LULIN 0.4-m telescope, 2015-07-25, $r_h = 1.26$ au inbound; (c) CAHA 3.5-m telescope, 2015-08-18, $r_h = 1.24$ au outbound; (d) OSN 1.52-m telescope, 2015-09-24, $r_h = 1.35$ au outbound; (e) OSN 1.52-m telescope, 2015-10-16, $r_h = 1.46$ au outbound; (f) CAHA 2.2-m telescope, 2015-11-05, $r_h = 1.61$ au outbound; (g) CAHA 2.2-m telescope, 2015-12-19, $r_h = 1.92$ au outbound; (h) CAHA 2.2-m telescope, 2016-03-29, $r_h = 2.69$ au outbound. North is up, and east to the left in all images. The directions of Sun and the negative of the comet's heliocentric velocity vector ($-v$) are drawn.

expected (Bentley et al. 2015). In fact, most particles analysed to date with that instrument have been described as hierarchical agglomerates of tens of microns in size, most of them compact, but a very fluffy one, with sub-unit size distributions with mean sizes near 1.5 μm (Mannel et al. 2016). The maximum size is considered to be time-dependent between a minimum of 1 cm as found by Rotundi et al. (2015) at far heliocentric distances pre-perihelion, and increasing up to 40 cm near perihelion, symmetrically distributed around perihelion. OSIRIS images have revealed the presence of decimetre-sized aggregates being ejected from the nucleus, from which a sizable amount (10 per cent or more) are believed to leave the nucleus gravity field (Agarwal et al. 2016). Single-particle detections by OSIRIS have revealed the presence of particles of masses of up to 100 kg, i.e. larger than 30 cm for our assumed density of 800 kg m^{-3}, and boulders of 40 cm in radius (Fulle et al. 2016a). The sensitivity of the model results to such large particles is dependent on the steepness of the size distribution function. The particle size distribution is assumed to be described by a power-law function. For particles larger than $r = 1$ mm, Fulle et al. (2016a) and Ott et al. (2017) found a considerably shallower size distribution than that found by dust trail modelling (a power index value of −4.1; see Agarwal et al. 2010), although approaching that value or even having lower values for the largest mass bins examined (particles with masses larger than 1 kg). We then assumed an intermediate value for the power index of $\alpha = -3.6$, which we adopted in our model for the current orbit. For particles smaller than 1 mm in radius, the index of the power law is taken as $\alpha = -3$ in the 4.5–2.9 au heliocentric distance range, as was determined from the Monte Carlo dust tail fitting of the VLT and OSIRIS data in that range (Moreno et al. 2016a). This index of $\alpha = -3$ is very close to the value reported by Hilchenbach et al. (2016) from COSIMA (the Cometary Secondary Ion Mass Analyser; Kissel et al. 2007) of $\alpha = -3.1$ in the heliocentric range between 3.6 and 3.1 pre-perihelion for particles in the 14 μm (COSIMA resolution limit) to the submillimeter domain, and is also in line with the estimates from ground-based dust tail modelling during previous orbits (Fulle et al. 2010). It is however steeper than that found from OSIRIS and GIADA data pre-perihelion ($\alpha = -2$; see Rotundi et al. 2015). This

discrepancy has been explained by the presence of a small population of fluffy particles with masses 10^{-11}–10^{-6} kg contributing to about 15 per cent of the coma brightness (Fulle et al. 2016a). Following the argument by Fulle et al. (2016a), we link the size distribution function to the nucleus seasons, so that we extend this value of $\alpha = -3$ to the whole southern hemisphere winter period (i.e. from aphelion to 1.7 au inbound, and from 2.6 au outbound to aphelion). During the nucleus southern hemisphere summer, i.e. from 1.7 au inbound to 2.4 au outbound, the size distribution power index is constrained together with the dust loss rate so as to satisfy the requirement that the integrated brightness in a certain aperture of both the observed and synthetic images are the same, i.e. the Afρ parameter at a certain ρ are the same. For the rest of the orbit (nucleus southern hemisphere winter), only the dust loss rate needs to be fitted because the size distribution is already fixed at $\alpha = -3$.

The terminal velocity function of the particles is parametrized as the product of a β-dependent function and a time-dependent function $u(t)$ as:

$$v(\beta, t) = \beta^{\gamma} u(t). \quad (1)$$

The exponent γ is taken as $\gamma = 0.5$, following dust drag models (e.g. Wallis 1982) and assuming that the grain mass m is related to its cross-section σ as $m \propto \sigma^{3/2}$ (Fulle et al. 2010). This value of $\gamma = 0.5$ is within the limiting values reported for this quantity from GIADA estimates (which ranged from 0.42 to 1.5; Della Corte et al. 2015, 2016). For the time-dependent function $u(t)$, we rely on the GIADA measurements. Della Corte et al. (2016) report the velocities of ejected particles measured by GIADA as a function of the heliocentric distance and illumination conditions. The range of particle masses collected is $2.8\times\ 10^{-9}$ to $1.4\times\ 10^{-6}$ kg, i.e. sizes ranging from effective radii 90 to 750 μm for the adopted $\rho_{\rm d} = 800$ kg m^{-3}. The observations were grouped into four observation periods, centred at heliocentric distances of 2.95 and 2.25 au pre-perihelion, perihelion, and 1.85 au post-perihelion. The measurements were fitted to power laws of the form:

$$v = Bm^{\gamma_m}, \quad (2)$$

where v is the velocity, m is the particle mass and B is a constant. The exponent γ_m and the constant B are functions of the observation period and the phase angle. To build up the terminal velocity of the particles in our model, as a function of the particle size and heliocentric distance, we used the mean values of B for each period, with a constant $\gamma_m = -0.32 \pm 0.18$, which was derived earlier by Della Corte et al. (2015), and which is consistent with all the values corresponding to the different heliocentric distances. For a particle radius of $r = 100$ μm, which is within the range of sizes detected by GIADA, the resulting velocity as a function of the heliocentric distance is given in Fig. 2.

The size dependence of the velocity we use applies strictly to the range of particle radii detectable by GIADA. An extrapolation of this law outside that range of sizes would be meaningless, as the velocities could result in unrealistic values. For example, if a particle of $r = 1$ μm at perihelion were emitted, it would get a velocity of 2.1 km s^{-1}, which is higher than expected even for gas atoms. We stick to the aforementioned dependence of v on β and time (equation 1). We fit the heliocentric (or time) dependence of the velocity with the log-normal function (see Fig. 2):

$$u(t) = K \exp \frac{-(\ln|t - 1100| - \mu)^2}{2\xi^2}, \quad (3)$$

where K, μ and ξ are constants and t is the time to perihelion expressed in days. The values of the constants are $K = 292$ and

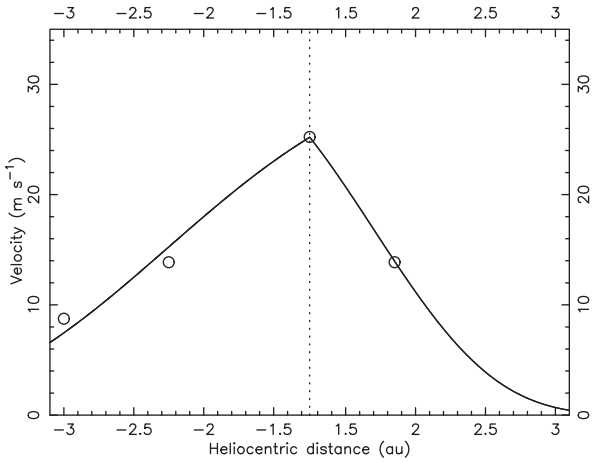

Figure 2. The adopted time dependence of the terminal velocity of grains of 100 μm in radius (solid line), as given by expression 3, compared with GIADA measurements (Della Corte et al. 2016) at different heliocentric distances (open circles).

$\mu = 7.003$. In order to fit the GIADA data properly, the function must be asymmetric with respect to perihelion. This is accounted for by the value of ξ, which is $\xi = 0.12$ pre-perihelion and $\xi = 0.082$ post-perihelion. The expression is always limited to the time span $t \geq 570$ d pre-perihelion, when we assume that the comet activity started, based on our previous results (Moreno et al. 2016a). For the minimum size allowed in the model, $r = 10$ μm, the ejection velocity at perihelion is ~ 80 m s^{-1}. The minimum values for the particle velocities should exceed the escape velocity (about $\sim$0.25 m s^{-1} at $\sim 20 R_{\rm N}$, where the gas drag is assumed to vanish). Since most of the largest particles are found to move radially with a velocity close to 1 m s^{-1} (Ott et al. 2017), we adopted that value as the minimum value for the velocity. Whenever the above equations give a particle velocity smaller than this minimum, we set the velocity to 1 m s^{-1}.

Since the observations cover a broad range of heliocentric distances, where the comet activity varies from nearly absent to a maximum near perihelion, the nucleus brightness has also been taken into account in the calculations. This was accomplished by an approximate model in which the nucleus is assumed spherical with an effective radius of 1.8 km, a geometric albedo of 0.065 and a linear phase coefficient of 0.047 mag deg^{-1} (Fornasier et al. 2015).

With the assumptions given so far, the only remaining input model parameter is the dust mass loss rate as a function of the heliocentric distance, and the power-law index of the size distribution function during the nucleus southern hemisphere summer. These functions are necessarily obtained by trial and error. To start the procedure, we use estimates based on the GIADA model (Fulle et al. 2010) and on the combined analysis of OSIRIS and VLT images at far pre-perihelion distances (Moreno et al. 2016a). As mentioned before, all the observations are calibrated so that the magnitudes in a 10^4 km aperture radius are coincident with those obtained by Snodgrass et al. (2016). Our modelled images are then forced to match as closely as possible the Afρ parameter obtained from the magnitude light curve at the corresponding heliocentric distances. This ensures that the observed and modelled images will have the same integrated brightness in the 10^4 km circular aperture region, at each observation date.

The computing time for the dust tail model is a growing function of the image dimensions. Since the amount of images to model is very large, we needed to rebin the images to dimensions such that the

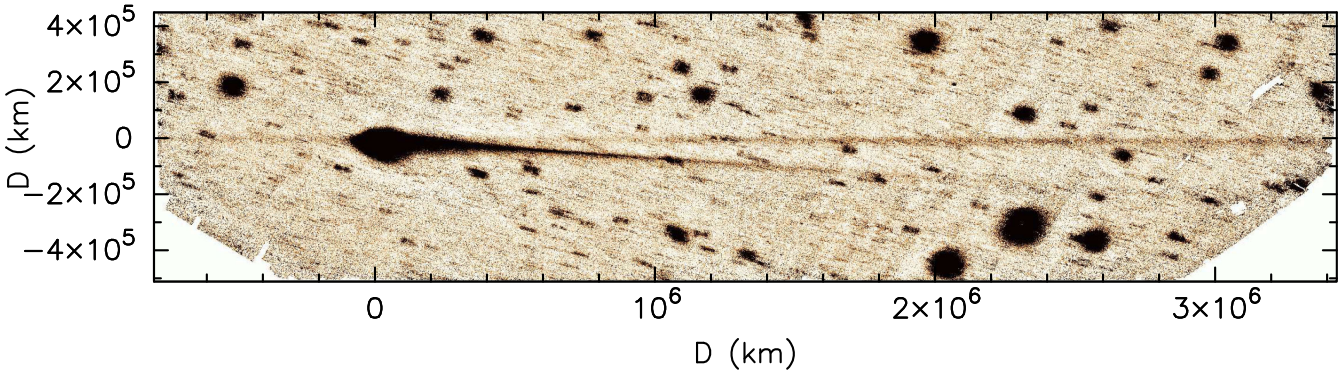

Figure 3. Trail and neck-line image of comet 67P obtained on 2016 March 8, using the Hyper Suprime-Cam (HSC) on the 8.2-m Subaru telescope. The image is oriented so that the trail appears horizontally. The horizontal dimension is 62.7arcmin, or, equivalently, 4.22×10^6 km. The image has been rebinned by 11 px for the purpose of modelling.

problem becomes tractable. Except for the VLT and LULIN images, for which the dust tails actually occupy a small area of pixels, the rest have been rebinned so that the final scales range from about 1.8 to 4.2arcsec px^{-1}, depending on the instrumental setup.

3.1 Trail modelling

Dust trails provide information on the large grain population ejected from the nucleus. Large grains are ejected at low velocities and are quite insensitive to solar radiation pressure, so that they remain for a long time close to the orbit of the comet, forming a linear and narrow dust structure. For 67P, the trail has been observed during past orbits (e.g. Ishiguro 2008; Agarwal et al. 2010; Tubiana et al. 2011). During the current orbit, we observed this structure from Subaru's 8.2-m telescope, as shown in Fig. 3. The image has been rotated so that the trail appears horizontally, while the neck-line appears oriented towards a direction south of the trail, allowing to analyse both features independently.

In addition to the current orbit, we also computed the trail brightness corresponding to observations acquired during previous orbits, in both the visible and the infrared. This provides us with stronger constraints on the retrieved dust parameters and gives additional confidence on the obtained results.

The particles composing the trail have been ejected for many years until the date of the observation. The maximum age of the trail is limited by the comet's orbital evolution, however. Most Jupiter Family Comets, and 67P in particular, have suffered close encounters with Jupiter in the past, implying significant changes in their orbital parameters. Comet 67P had a close encounter with the planet in early 1959. To quantify the magnitude of the changes in the orbital parameters before and after the encounter, we have performed a backward-in-time integration of the nominal 67P orbit using the Mercury package (Chambers 1999) with the Burlish–Stoer integrator. Fig. 4 shows the time evolution of the perihelion distance (q) and the inclination (i). The 1959 Jupiter encounter, in which the comet passed at only 0.053 au from the planet, reduced the perihelion distance from $q = 2.74$ au to $q = 1.29$ au, and the inclination from $i = 23$ deg to $i = 7$ deg. Then, the computations related to the trail should begin in 1959, because older particles have followed other orbital paths and do not contribute to the current trail brightness. In addition, there is also a small jump in perihelion distance from about 1.29 au to the current 1.243 au occurring during late 2007 that has also been taken into account when considering the dust loss rates at different epochs.

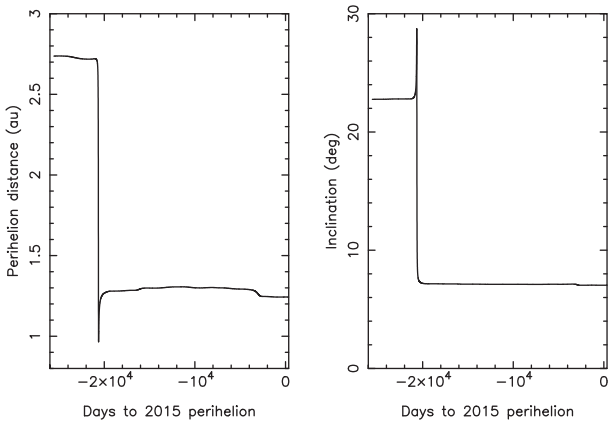

Figure 4. Perihelion distance (q) and inclination (i) of the orbit of 67P backward in time since the current perihelion passage. The sudden jump in both q and i occurred because of a close encounter with Jupiter in 1959 February, when the comet passed at only 0.053 au from the planet.

The dust trail simulations in the visible range of the spectrum are performed in the same way as in the current orbit image simulations, but adding up to the modelled image brightness the contribution of the particles ejected back to 1959. To keep the time-step used for the current orbit model, the computational time spent to generate the trail image increases by a factor proportional to the number of revolutions of the comet around Sun (i.e. a factor ∼10).

In the infrared range, we followed the same procedure, but taking into account that the flux of each particle in this case is given by:

$$F_\lambda = \frac{a^2}{\Delta^2}\epsilon(\lambda, a)\pi B_\lambda[T(a)], \tag{4}$$

where λ is the wavelength, Δ is the geocentric distance, a is the grain radius, ϵ is the grain emissivity, B_λ is the Planck function and $T(a)$ is the grain equilibrium temperature. This temperature can be computed by the balance between the absorbed solar and emitted thermal radiation as:

$$T(a) = 278.8\left(\frac{1 - A_B}{\epsilon}\right)^{1/4}\frac{1}{r_h}, \tag{5}$$

where A_B is the Bond albedo of the grains and r_h is the heliocentric distance, in au. As in Agarwal et al. (2010), we adopted $\epsilon/(1 - A_B) = 0.62 \pm 0.2$ from *IRAS* measurements (Sykes & Walker 1992).

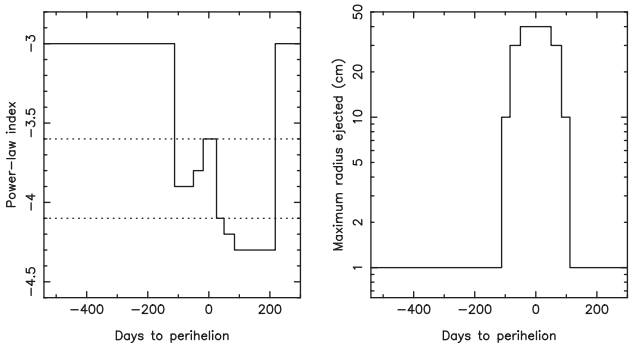

Figure 5. Left-hand panel: time evolution of the power index of the size distribution function. The solid line corresponds to particles of radii smaller than 1 mm. The large particles, with $r > 1$ mm, are characterized by a size distribution with a constant power index of −3.6 for the current orbit, and of −4.1 for all the orbits previous to the 2009 perihelion passage (dotted lines). Right-hand panel: the modelled maximum ejected particle radius as a function of the time to perihelion passage.

4 RESULTS AND DISCUSSION

In order to find the dust loss rate as a function of the heliocentric distance, we start at the earliest date in the current orbit, i.e. some 570 d pre-perihelion, as stated before. To perform this, we have the previous estimates of the dust loss rate profile we obtained from combined VLT and OSIRIS data at large heliocentric distance (Moreno et al. 2016a). However, in that case we assumed different input model parameters concerning the particle density (2000 kg m^{-3}), the minimum particle size (1 μm versus 10 μm in this model) and the terminal velocity that was assumed as a random distribution based on the results by Rotundi et al. (2015), so that the profile cannot be directly taken from that model, although it certainly provides a first approximation. In addition, the heliocentric dependence of the power index of the size distribution during the nucleus southern hemisphere summer must also be found. The best-fitting dust loss rates and power index functions are found by trial and error, always trying to satisfy the criterion that the Afρ parameter obtained from the synthetic images matched that of the experimental results (for a $\rho = 10^4$ km aperture radius). The resulting model size distribution and the variation of particle size as a function of time to comet's perihelion are shown in Fig. 5. The size distribution during the nucleus southern hemisphere summer is much steeper than that during the nucleus southern hemisphere winter, with power indices ranging between −3.7 and −4.3. This is consistent with the increase of slope in the size distribution found by GIADA, showing a value of −3.7 at perihelion (Della Corte et al. 2016; Fulle et al. 2016a).

The obtained values of Afρ from the synthetic images are compared with the experimental values in Fig. 6, showing an excellent agreement. In that plot, the phase angle as a function of time is also displayed, just to show that the small secondary maxima in Afρ correlate with small phase angle domains, near −400 and +200 d to perihelion, a characteristic feature of the backscattering enhancement of the dust phase function, that is being modelled using a linear phase coefficient as described above.

The obtained dM/dt profile, shown in Fig. 7, where also the water production rate is plotted, shows a maximum at ∼3100 kg s^{-1} at 20 d after perihelion, and an asymmetric shape, showing a faster decay post-perihelion. The outburst that occurred during the *Rosetta* approach phase on 2014 April 30 (470 d to perihelion, at 4.11 au inbound; Tubiana et al. 2015; Moreno et al. 2016a) is clearly

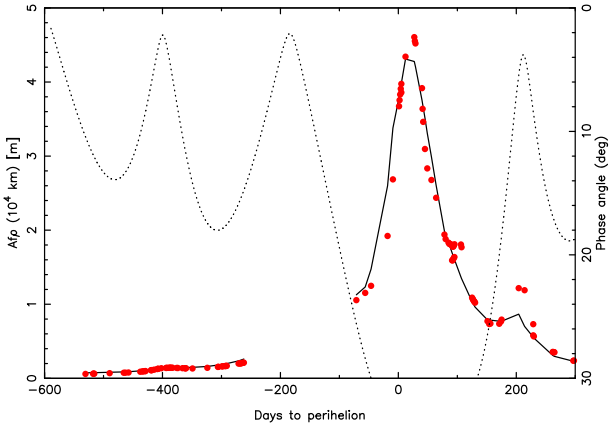

Figure 6. The variation of the Afρ parameter, at a 10^4 km aperture radius, with respect to time to perihelion. The solid black line corresponds to the observations, and the red solid circles are the computed Afρ on the synthetic images. The dotted line is the solar phase angle of the comet. The small secondary maxima in Afρ, correlated with small phase angle domains, near −400 and +200 d to perihelion, are a characteristic feature of the backscattering enhancement of the dust phase function.

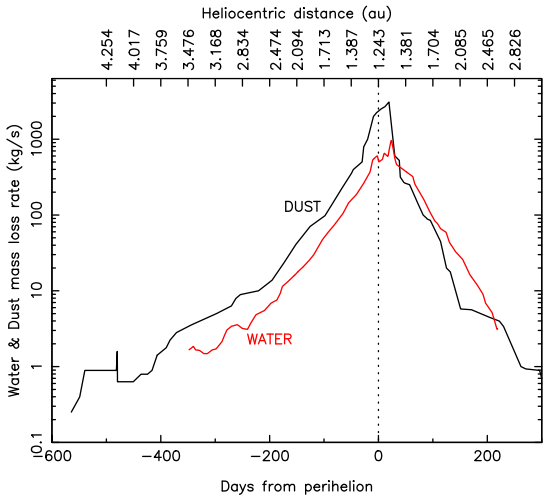

Figure 7. Modelled dust loss rate (black line) and water production rate (red line) from ROSINA instrument on board *Rosetta* (Hansen et al. 2016), as a function of the heliocentric distance. The sudden increase in dust loss rate at 470 d pre-perihelion (4.11 au) for the modelled dust loss rate corresponds to the outburst observed by the OSIRIS camera on 2014 April 30 (Tubiana et al. 2015; Moreno et al. 2016a).

mimicked by the model by a moderate increment followed by a sharp increase in dM/dt.

The isophote fields of the modelled images are compared with the observations in Fig. 8. To save space, we only provide a representative subset of 16 images out of the 116 modelled images.

The modelled isophotes agree well in general with the observations, mainly in the innermost, densest regions of the images where most of the flux is concentrated. This is consistent with the good fit to the measured Afρ values, as shown above (see Fig. 6). The outermost modelled isophotes display divergences with the observed images, especially near perihelion. This is mostly due to the assumed isotropic ejection pattern, that tends to circularize the isophote contours.

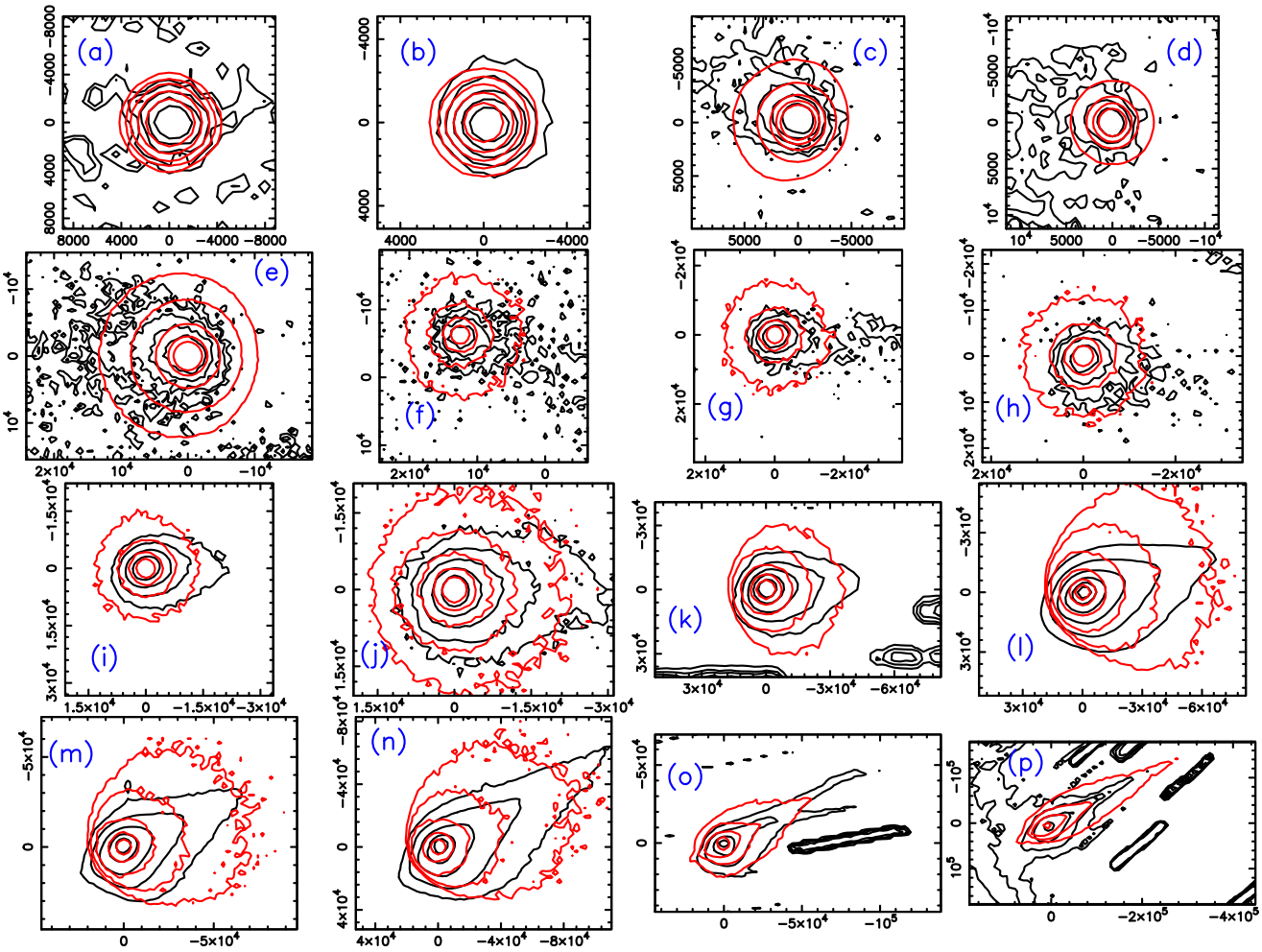

Figure 8. Isophote fields of a subset of observed (black contours) and modelled images (red contours) at different heliocentric distances (in au), and having the following values for the innermost isophote (in solar disc units), respectively: (a)−4.33, 1.63×10^{-14}; (b)−3.80, 1.18×10^{-13}; (c)−3.54, 4.30×10^{-14}; (d)−3.20, 6.24×10^{-14}; (e)−2.95, 4.33×10^{-14}; (f)−1.51, 5.10×10^{-13}; (g)−1.42, 7.68×10^{-13}; (h)−1.37, 9.95×10^{-13}; (i)−1.27, 1.63×10^{-12}; (j)−1.25, 2.29×10^{-12}; (k)+1.25, 1.62×10^{-12}; (l)+1.30, 2.21×10^{-12}; (m)+1.47, 7.94×10^{-13}; (n)+1.62, 4.18×10^{-13}; (o)+2.69, 3.99×10^{-14}; (p)+3.14, 1.05×10^{-14}. Negative distances indicate pre-perihelion, positive post-perihelion. Isophotes decrease by factors of 2 outwards. The *x*- and *y*-axes are all labelled in km projected at the comet distance. All images are shown in the conventional North-up and East-to-the-left orientation.

4.1 Comparison of dust to water production rates

The dust-to-gas mass ratio is an important parameter in the characterization of comets because it gives insights on their formation mechanisms and their evolution. Water production measurements of 67P along the current orbit have been provided by Hansen et al. (2016), using several instruments on *Rosetta* spacecraft, namely ROSINA (Rosetta Orbiter Spectrometer for Ion and Neutral Analysis), MIRO (Microwave Instrument for Rosetta Orbiter), VIRTIS (Visible InfraRed Thermal Imaging Spectrometer) and RPC (The Rosetta Plasma Consortium). Hansen et al. (2016) have shown (see their fig. 9) that the water production rate is highly correlated with scaled (arbitrary units) ground-based magnitude measurements. Hansen et al. (2016) stated that this correlation possibly indicates that several dust parameters are constant during the observed period. However, based mostly on GIADA data and the model results, this is not the case, because both the size distribution and the particle velocities are functions of the heliocentric distance (Fulle et al. 2016a; Della Corte et al. 2015, 2016), so that the striking correlation between Afρ and water production must be explained in another way. We note that this correlation is in line with that reported by Jorda et al. (2008) of visual magnitudes and water production rates of a sample of comets, which, to our knowledge, has not been explained yet, requiring further modelling. In Fig. 7, we compare the ROSINA water production rates extracted from a digitization of Fig. 6 in Hansen et al. (2016) with the dust production rate obtained in our nominal model. As it is seen, both curves are not well correlated, the gas and dust production rates varying differently with time, indicating a non-constant dust-to-gas ratio. The use of the Afρ parameter that can be derived from the magnitude data, as a proxy of the dust production rate, a common assumption by many authors, is not justified for various reasons. First, the Afρ parameter has dimensions of length, while production rate has dimensions of mass per unit time. Secondly, only in the hypothetical case in which both the particle velocity and the size distribution are time-independent the same time evolution of Afρ and dust loss rate is expected (Fulle 2000). In addition, and on a very fundamental level, the dust mass loss rate is an instantaneous quantity while the Afρ parameter depends on the amount, size and velocity of particles ejected from the nucleus at times *before* the observation. For instance, on a highly hypothetical case in which a nucleus stops emitting particles, the

Afρ parameter will still give non-zero values for some time, i.e. till when all particles leave the aperture. Another example is related to the neck-line structure. In a post-perihelion image, the neck-line particles are always contributing in a non-negligible amount to the brightness in the near-nucleus region. Those particles were in fact emitted quite a long time before the observation (or the order of several months or more), so that the instantaneous dust loss rate and the Afρ parameter at any post-perihelion date can only be related in a very complicated way. The brightness contribution to the nucleus at far distances from perihelion contributes in fact to the Afρ parameter, but it is independent of the dust loss rate.

Taking into account the results of the model shown in Fig. 7, the resulting total dust mass ejected becomes 1.4×10^{10} kg. Taking into account the integrated water production during an orbit of $(2.7 \pm 0.4) \times 10^{9}$ kg by Bertaux (2015), we obtain a dust-to-gas mass ratio of d/g $\sim$ 5. This ratio is smaller if we consider the total gas mass (all gases) ejected of 7.9×10^{9} to 9.2×10^{9} kg as estimated by Hansen et al. (2016), so that d/g would actually vary between 1.5 and 1.8.

4.2 Trail data fitting

As mentioned before, the trail data that are being modelled refer to the current orbit as well as to images acquired during previous orbits, with observation dates in 2006 April and earlier. The dust production rates and particle size distribution might have changed among different comet orbits. In fact, some orbital parameters have shown slight changes with time since 1959, the latest Jupiter close encounter. For instance, the perihelion distance until late 2007 was $q \sim 1.29$ au, while on 2009 and the current 2015 perihelia $q \sim 1.24$ au (see Fig. 4). For the trail simulations, we assumed that the dust parameters inferred for the current orbit are valid backwards in time until late 2007. Back from that date, we assumed the size distribution at $r > 1$ mm as was already derived by Agarwal et al. (2010) in their analysis of old trail data, i.e. a power law characterized by an index of -4.1. The remaining dust parameters were assumed as those derived for the current orbit, but taking into account the dependence of dust loss rate as a function of the heliocentric distance displayed in Fig. 7. Owing to the strong variation of dust loss rate with heliocentric distance, the peak loss rate for perihelia older than that of 2009 is $\sim$700 kg s^{-1}, i.e. a factor of $\sim$4 smaller with respect to the 2015 and 2009 perihelia.

Under the above-described hypothesis, the result of the computations for the Subaru image is shown in Fig. 9. As it is seen, the simulations reproduce reasonably well the observed trail brightness except in the vicinity of the coma behind the comet. However, this brightness decrease is not observed in any other of the trail data analysed, which might indicate some sensitivity problem in the corresponding area of the detector, as the brightness level is close to the background noise. The observations of the dust trail by Tubiana et al. (2011) with VLT/FORS2 and a red filter in 2004 April do not display such brightness decrease, showing a much more uniform distribution (see Fig. 10). As before, the model simulation agrees well with the observation, although the portion of the simulated trail ahead of the comet is brighter than the data. The same effect is seen on the simulations of the *Spitzer*/MIPS images at 24 μm by Agarwal et al. (2010), specifically those corresponding to 2005 August 28–29 and 2006 April 8–9 (see Fig. 11). In any case, the agreement of the simulations with all the trail data is in general very good, confirming the adequacy of the model parameters.

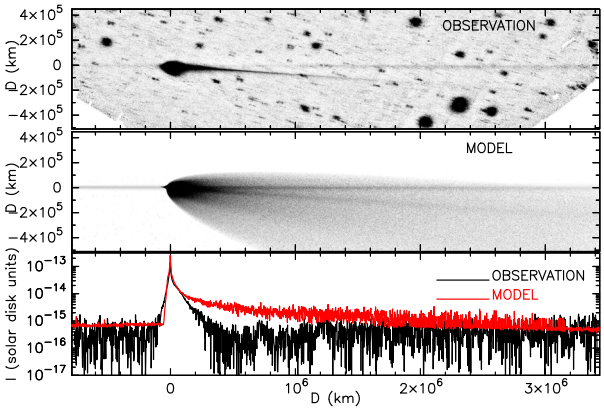

Figure 9. Observed (top panel) and modelled (middle panel) images of comet 67P on 2016 March 8. The lowermost panel shows the observed (black line) and modelled (red line) scans along the trail. The scale in the *y*-axis in this panel is given in solar disc intensity units.

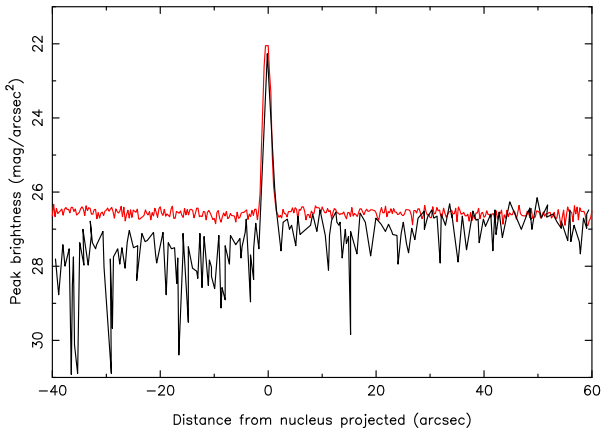

Figure 10. Brightness along the trail for the 67P 2004 April image, obtained at a heliocentric distance of 4.67 au, by Tubiana et al. (2011). The black line corresponds to the observational data, digitized from their Fig. 10, and the red line is the modelled scan. The nucleus brightness emerges at the corresponding position.

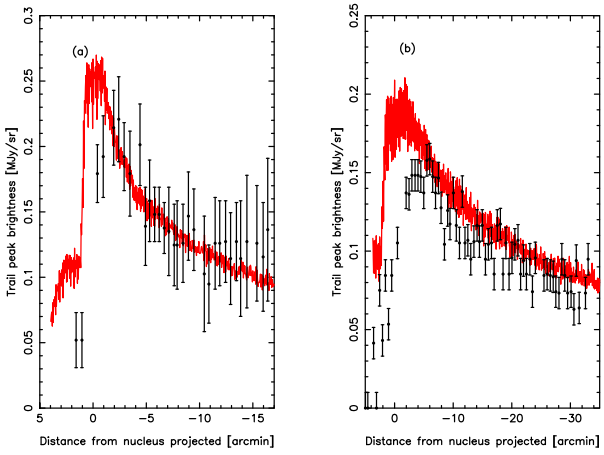

Figure 11. Peak brightness along the observed trail in the MIPS24 channel of *Spitzer* digitized from Agarwal et al. (2010) (solid circles with error bars, corresponding to their figs 2 and 3). The red solid lines are the modelled peak brightness along the simulated trails. Panel (a) corresponds to the observations on 2005 August 28–29, and panel (b) to the observations on 2006 April 8–9.

5 CONCLUSIONS

We have described and analysed with dust tail models an extensive data set of images of comet 67P, covering a large portion of the orbital arc between 4.5 au pre-perihelion and 3 au post-perihelion. The retrieved model parameters are based on the interpretation of such a set of well-calibrated images, as well as from trail observations during this and previous orbits, in both the visible and the infrared.

The main conclusion is that the results on dust properties derived from the ground for the current orbit are found to be consistent with those reported from the *Rosetta in situ* instruments. The particle velocities are compatible with those retrieved from the instrument GIADA. The minimum particle radius of 10μm and the maximum of 40 cm are the lower and upper limiting sizes found by MIDAS and OSIRIS. For particles with radii $r < 1$ mm, the size distribution function is related to 67P nucleus seasons; it is characterized by a power-law index of -3 during the long southern hemisphere winter, and by a much steeper index ranging between -3.7 and -4.3 during the perihelion southern hemisphere summer (from 1.7 au inbound to 2.6 au outbound). For particles larger than 1 mm, we assumed a power index of -3.6, independently of the heliocentric distance. This is a value consistent with OSIRIS mean results (Fulle et al. 2016a; Ott et al. 2017) at perihelion. The peak loss rate is $\sim$3000 kg s^{-1}, which is of the order of, although smaller than, the perihelion loss rate inferred from single-particle detections from OSIRIS, in the range 5000–8000 kg s^{-1} (Fulle et al. 2016a; Ott et al. 2017).

For the analysis of the trail data, we assumed a power-law index for the size distribution of large particles ($r > 1$ mm) of -4.1 for all epochs back from late 2007, in agreement with the findings based on old trail data analysis (Agarwal et al. 2010). In addition, the perihelion peak dust production rate is lower in a factor of $\sim$4 during epochs earlier than 2007 than in the 2009 and the current 2015 perihelion because of the larger perihelion distance at earlier epochs. The quality of the fits to the current orbit observations, as well as to trail data during this and previous orbits, confirms the suitability of the dust model parameters. Processes such as grain fragmentation, sublimation, electrostatic disruption or any other mechanism involving particle size evolution, once the grains reach distances far away from the circumnuclear region, do not seem to play a significant role.

ACKNOWLEDGEMENTS

We are very grateful to an anonymous referee for her/his appropriate and constructive comments that helped to improve the paper considerably.

This work was supported by contracts AYA2015-67152-R, AYA2015-71975-REDT and ESP2014-54032 from the Spanish Ministerio de Economía y Competitividad, and I/032/05/0 and I/024/12/0 from the Italian Space Agency (ASI).

This paper is based on observations made with ESO telescopes at the La Silla Paranal Observatory under programmes IDs 592.C-0924, 093.C-0593 and 094.C-0054. It is also based on observations collected at the Centro Astronómico Hispano-Alemán (CAHA) at Calar Alto, operated jointly by the Max-Planck Institut fuer Astronomie and the Instituto de Astrofísica de Andalucía (CSIC), and on data obtained at the Observatorio de Sierra Nevada, which is operated by the Instituto de Astrofísica de Andalucía (CSIC).

REFERENCES

A'Hearn M. F., Schleicher D. G., Millis R. L., Feldman P. D., Thompson D. T., 1984, AJ, 89, 579
Agarwal J., Müller M., Reach W. T., Sykes M. V., Boehnhardt H., Grün E., 2010, Icarus, 207, 992
Agarwal J. et al., 2016, MNRAS, 462, 78
Bentley M. S., Torkar K., Jeszenszky H., Romstedt J., Schmied R., Mannel T., 2015, Eur. Planet. Sci. Congr., 10, 441
Bertaux J.-L., 2015, A&A, 583A, 38B
Chambers J. E., 1999, MNRAS, 304, 793
Colangeli L. et al., 2007, Space Sci. Rev., 128, 803
Della Corte V. et al., 2015, A&A, 583, A13
Della Corte V. et al., 2016, MNRAS, 462, 210
Fornasier S. et al., 2015, A&A, 583, 30
Fulle M., 1989, A&A, 217, 283
Fulle M., 2000, Icarus, 154, 239
Fulle M. et al., 2010, A&A, 522, A63
Fulle M. et al., 2016a, ApJ, 821, 19
Fulle M. et al., 2016b, MNRAS, 462, 132
Hansen K. C. et al., 2016, MNRAS, 462, 491
Hilchenbach M. et al., 2016, ApJ, 816, L32
Ishiguro M., 2008, Icarus, 193, 96
Jorda L., Crovisier J., Green D. W. E., 2008, LPI Contrib. 1405, 8046
Keller H. U. et al., 2007, Space Sci. Rev., 128, 433
Kissel J. et al., 2007, Space Sci. Rev., 128, 823
Lara L. M. et al., 2015, A&A, 583, A9
Lin Z.-Y. et al., 2015, A&A, 583, A11
Mannel T., Bentley M. S., Schmied R., Jeszenszky H., Levasseur-Regourd A. C., Romstedt J., Torkar K., 2016, MNRAS, 462, 304
Meech K. J., Jewitt D. C., 1987, A&A, 187, 585
Moreno F., Pozuelos F., Aceituno F., Casanova V., Sota A., Castellano J., Reina E., 2012, ApJ, 752, 136
Moreno F. et al., 2016a, A&A, 587, A155
Moreno F., Licandro J., Cabrera-Lavers A., Pozuelos F. J., 2016b, ApJ, 826, L22
Ott T. et al., 2017, MNRAS, this issue
Riedler W. et al., 2007, Space Sci. Rev., 128, 869
Rotundi A. et al., 2015, Science, 347, aaa3905
Snodgrass C. et al., 2016, A&A, 588, A80
Snodgrass C. et al., 2017, Phyl. Trans. R. Soc. A, 375, 20160249
Sykes M. V., Walker R. G., 1992, Icarus, 95, 180
Tubiana C., Böhnhardt H., Agarwal J., Drahus M., Barrera L., Ortiz J. L., 2011, A&A, 527, A113
Tubiana C. et al., 2015, A&A, 573, A62
Vincent J.-B. et al., 2016, A&A, 587, A14
Wallis M. K., 1982, In: Comets. Univ. Arizona Press, Tucson, AZ, p. 357

SUPPORTING INFORMATION

Supplementary data are available at *MNRAS* online.

Table 2. Log of the observations.

Please note: Oxford University Press is not responsible for the content or functionality of any supporting materials supplied by the authors. Any queries (other than missing material) should be directed to the corresponding author for the article.

This paper has been typeset from a TEX/LATEX file prepared by the author.